

Improving Lesion Segmentation in Medical Images by Global and Regional Feature Compensation

Chuhan Wang^a, Zhenghao Chen^b, Jean Y. H. Yang^c, Jinman Kim^{a,*}

^a*Biomedical Data Analysis and Visualisation (BDAV) Lab, School of Computer Science, Faculty of Engineering, The University of Sydney, Sydney, 2008, NSW, Australia*

^b*School of Information and Physical Sciences, The University of Newcastle, Newcastle, 2308, NSW, Australia*

^c*School of Mathematics and Statistics, Faculty of Science, The University of Sydney, Sydney, 2006, NSW, Australia*

Abstract

Automated lesion segmentation of medical images has made tremendous improvements in recent years due to deep learning advancements. However, accurately capturing fine-grained global and regional feature representations remains a challenge. Many existing methods obtain sub-optimal performance on complex lesion segmentation due to information loss during typical downsampling operations and the insufficient capture of either regional or global features. To address these issues, we propose the Global and Regional Compensation Segmentation Framework (GRCSF), which introduces two key innovations: the Global Compensation Unit (GCU) and the Region Compensation Unit (RCU). The proposed GCU addresses resolution loss in the U-shaped backbone by preserving global contextual features and fine-grained details during multiscale downsampling. Meanwhile, the RCU introduces a self-supervised learning (SSL) residual map generated by Masked Autoencoders (MAE), obtained as pixel-wise differences between reconstructed and original images, to highlight regions with potential lesions. These SSL residual maps guide precise lesion localization and segmentation through a patch-based cross-attention mechanism that integrates regional spatial and pixel-level features. Additionally, the RCU incorporates patch-level importance scoring to enhance feature fusion by leveraging global spatial information from the backbone. Experiments on two publicly available medical image segmentation datasets, including brain stroke lesion and coronary artery calcification datasets, demonstrate that our GRCSF outperforms state-of-the-art methods, confirming its effectiveness across diverse lesion types and its potential as a generalizable lesion segmentation solution.

Keywords: Medical Image Processing, Lesion Segmentation, Global and Regional Feature, Representation Learning, Self-supervised Learning, Transformer, Mask Autoencoders

1. Introduction

In medical imaging, accurate lesion segmentation plays a critical role in assisting clinicians with diagnosing diseases, monitoring disease progression, and evaluating treatment effectiveness [1]. Despite advancements in automated segmentation methods, accurately localizing and delineating lesions with complex characteristics remains challenging [2]. For example, ischemic stroke lesions in the brain pose a significant segmentation challenge due to their low-contrast, where the pixel intensities are similar to those of the surrounding tissues, referred to as isointense [3] in MR imaging. The limitations of T1-weighted imaging to capture edema and early ischemic changes [4] make low-contrast stroke lesions difficult to distinguish from normal tissues. These lesions often exhibit irregular and ambiguous boundaries [5], further complicating their segmentation using traditional deep learning methods. Another example of challenging segmentation task is coronary artery calcification (CACs), occupying only a small region of the image, often measuring less than 5 mm in length and corresponding to 10–13 pixels referring to different in-plane resolution in the non-contrast CT slices used in this study [6]. The small size and irregular shape of the CACS, along with its variability in location and density, make precise segmentation and quantification difficult. Furthermore, non-contrast CT, the primary imaging modality for detecting and assessing CACS [7], further complicates the process due to its low signal-to-noise ratio, resulting in blurred boundaries and imprecise delineation.

Automated segmentation methods have improved significantly in recent years, driven by advances in deep learning [8, 9]. Convolutional neural networks (CNN) [10], particularly encoder-decoder architectures [11] such as U-Net [12] and UNet ++ [13], have been widely applied for medical image segmentation task. These architectures preserve regional context but failed to capture global context due to fixed-size convolutional kernels, limiting their ability to segment lesions with varying locations or ambiguous boundaries. To address these limitations, advanced CNN-based models, such as DeepLabv3 [14] implement various receptive fields to improve the segmentation of complex anatomical structures, but remain limited by the fundamental constraints of convolutional operations, particularly in modeling long-range dependencies.

In recent years, transformer-based models [16, 17, 18, 19, 20] have demonstrated their potential in addressing these limitations by modeling global context and capturing long-range de-

*Corresponding author: Email: jinman.kim@sydney.edu.au;

Email addresses: chuhan.wang@sydney.edu.au (Chuhan Wang), zhenghao.chen@newcastle.edu.au (Zhenghao Chen), jean.yang@sydney.edu.au (Jean Y. H. Yang), jinman.kim@sydney.edu.au (Jinman Kim)

dependencies through self-attention mechanisms. TransUNet [17] and SwinUNet [19] integrate hybrid architectures to learn regional and global characteristics, resulting in improved segmentation performance. However, they rely on skip connections to transfer low-level features from the encoder to the decoder for spatial detail recovery. This approach may not fully capture fine-grained details, limiting their localization ability and accuracy in segmenting challenging lesions. Several other transformer-based models [21, 22, 23] have been developed to solve the challenges of medical image segmentation. While these models have shown notable improvements in handling complex and variable structures, they still face challenges in accurately localizing subtle and irregular lesions and delineating their boundaries. This limitation arises because patch-based self-attention tends to blur regional details and introduce feature inconsistencies among patches. SPiN [24] is developed to address these challenges using the subpixel mechanism. Although effective in handling small stroke lesion segmentation, SPiN relies heavily on supervised learning approach and requires extensive manually annotated datasets.

Recent methods have enhanced performance in segmentation tasks by employing self-supervised learning (SSL) [25], which learns meaningful representations from unlabeled data. SSL reduces reliance on costly and time-intensive manual annotations while improving downstream task performance. It achieves this through pretext tasks that exploit the inherent structure of images, such as contrastive learning [26, 27, 28], pixel-level image reconstruction [29], and masked token prediction [30, 31]. These tasks enable models to extract robust global features [32, 33] from datasets and localized features from individual images, which can serve as initialization weights for supervised learning. SSL has demonstrated particular effectiveness in medical imaging [34, 35, 36], showing that SSL pre-training improves segmentation performance, especially when fine-tuned with small annotated datasets. However, many SSL methods focus predominantly on learning high-level global features that capture the overall data context, often overlooking fine-grained, pixel-level details. These details, critical for segmentation tasks, such as precisely delineating the boundaries of challenging lesions with low-contrast or small sizes, remain unexplored in existing SSL approaches. This gap underscores the need for SSL methods that integrate global and pixel-level information to enhance segmentation performance. Masked Autoencoders (MAE) [29], introduced by He *et al.*, addresses this limitation by incorporating localized feature representations. Although MAE has been used primarily as a pre-training technique in medical imaging [37, 38], its potential for tasks beyond pre-training, such as using

reconstructed images to guide segmentation remains unexplored.

To address the limitations mentioned above, we propose a novel dual-feature compensation framework, named Global and Regional Compensation Segmentation Framework (GRCSF), to improve the medical image segmentation of challenging lesions. GRCSF adopts an encoder-decoder structure built on UNet++ and takes the raw images as input. It compensates for the detailed global features that are often missing in CNN-based models. Unlike traditional approaches that use MAE for pre-training, our method, to our knowledge, is the first medical image segmentation framework to use MAE’s reconstruction process to generate SSL residual maps that capture pixel-level differences between the original images and their reconstructions. Therefore, it mitigates the inconsistency between global and local feature representations introduced by transformer models. The key contributions of our work are as follows:

- We introduce a novel medical image segmentation framework, namely, GRCSF, which exploits global and regional feature compensation strategies to produce better coarse-to-fine features and improve lesion segmentation.
- We introduce the Global Compensation Unit (GCU) module within the encoder, using feature recovery from the similarity of different scales. It updates skip connection features by using the global context and progressively refines the multi-scale features. It addresses the loss of detailed global features caused by downsampling and solves the problems of inaccurate boundary delineation and low sensitivity in segmenting complex lesions.
- We introduce the Regional Compensation Unit (RCU) module within the decoder, by applying a cross-attention mechanism on residual maps learned from the SSL strategy and the features of UNet++. We can obtain importance score maps to better highlight those regions with a higher likelihood of containing lesions by incorporating additional global features from the backbone model, which helps reduce false-positive regions on the SSL residual maps. The RCU addresses the challenge of localizing blurred lesions that are often difficult to detect based on limited regional spatial features.
- We validate the effectiveness and robustness of GRCSF for general lesion segmentation, using two representative datasets: ATLAS 2.0, which consists of low-contrast brain stroke lesions, and orCaScore, which contains small-sized coronary artery calcifications.

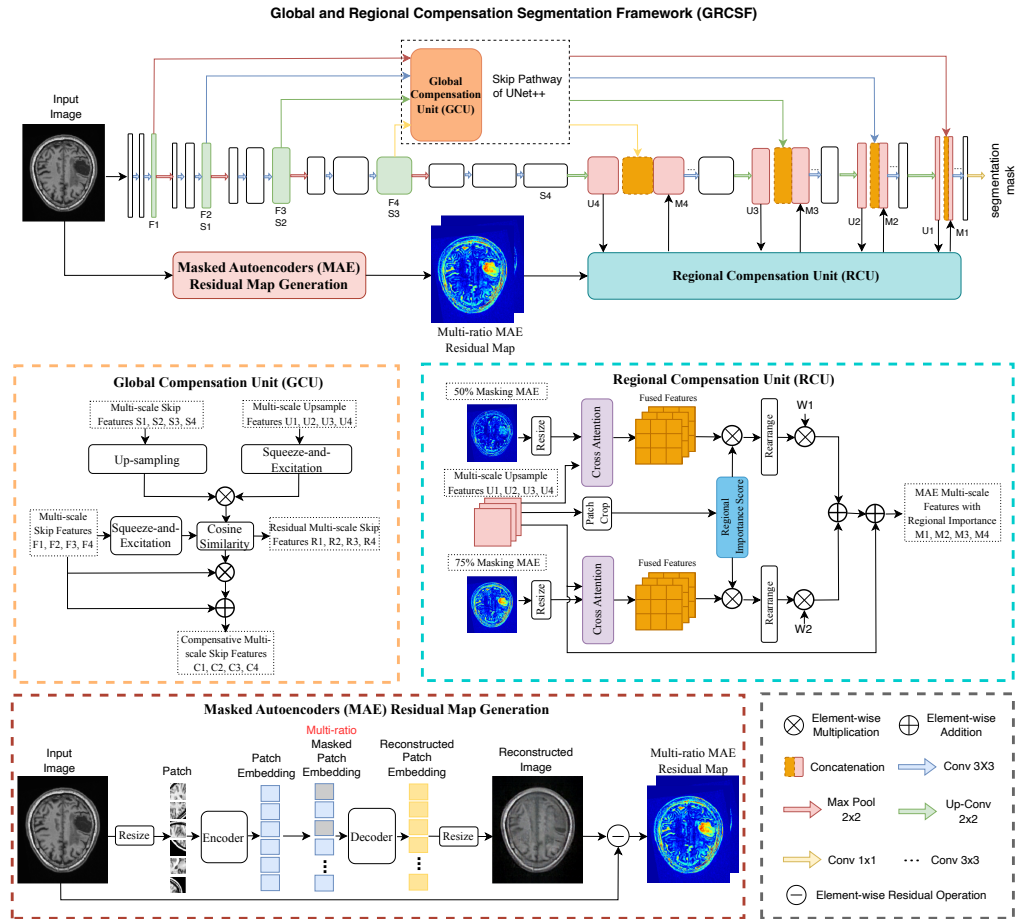


Figure 1: Overview of the GRCSF architecture. A U-shaped backbone network for medical image segmentation. The backbone integrates the Global Compensation Unit (GCU) within the skip connections and the Regional Compensation Unit (RCU) in the decoder layers. The masked Autoencoders (MAE) model was implemented using pre-trained weights for input size of 224x224. To ensure the correct input and output sizes, we resized the input images before and after processing through the MAE.

2. Related Work

2.1. Deep Learning for Supervised Medical Image Segmentation

The CNN-based encoder-decoder architectures [11] such as U-Net [12] and its variant UNet++ [13], have been widely adopted for the medical image segmentation task. These architectures utilize skip connections to preserve spatial resolution, making them effective for various segmentation tasks. Unet++ improved multi-scale feature extraction by introducing nested skip pathways, further enhancing its ability to handle complex and heterogeneous medical data. DeepLabv3 [14] introduced Atrous Spatial Pyramid Pooling (ASPP) [15] to encode multi-scale contextual information by probing features at multiple rates and fields of view. A recent study SPiN [24] has made efforts to accurately segment isointense brain stroke lesions. It developed a subpixel embedding mechanism to generate high-resolution confidence maps and employed a learnable downsampler to accurately localize irregular lesions and delineate boundaries. While CNN-based segmentation models have demonstrated improvement in medical image segmentation, they are still limited to capture global features due to fixed receptive field.

Transformer-based models TransUNet [17] combined CNNs and transformers in a hybrid architecture, leveraging CNNs for high-resolution spatial encoding and transformers for capturing long-range dependencies. Similarly, SwinUNet [19] adopted a fully transformer-based U-shaped model, incorporating a hierarchical Swin Transformer [20] with a shifted windows mechanism as the encoder to simultaneously model global and local dependencies. However, the use of window-based attention in transformer-based models can introduce boundary discontinuities, which is particularly problematic for lesions with ambiguous edges. Moreover, its performance is heavily dependent on large training datasets and extensive parameter tuning, making adaptation to new datasets challenging.

Existing methods either fail to effectively capture global features or lack consistency in regional feature representation. GRCSF utilizes pixel-level similarity from different feature scales to enhance feature representations.

2.2. Self-Supervised Learning for Medical Image Segmentation

SSL leverages unlabeled data to learn meaningful feature representations for different tasks. For example, MAE, originally developed for natural images, have also shown potential in medical imaging by reconstructing masked image patches and learning global semantic and localized

contextual features. MAE employs an encoder-decoder architecture where a portion of image patches is randomly masked during training. The encoder extracts semantic information from visible patches, while the decoder reconstructs the masked regions. This approach allows MAE to learn the overall structure of the dataset and the unique fine-grained details of each image. Zhou *et al.* [37] has shown that MAE self pre-training improves various medical image tasks, including abdominal CT multi-organ segmentation, and MRI brain tumor segmentation. Mask in Mask (MiM) [38] framework introduced hierarchical token learning and cross-level alignment mechanisms to improve downstream segmentation tasks across large-scale datasets.

These advances highlight the growing impact of SSL in medical image segmentation, enabling models to leverage unlabeled data effectively and generalize across diverse medical imaging tasks. However, most SSL methods remain primarily focused on pre-training. To our best knowledge, GRCSF is the first medical image segmentation work to exploit the capacity of SSL to recover global features and produce residual maps that highlight the regions of potential lesion used for regional feature compensation. This operation takes advantage of additional features to improve the likelihood at the pixel-level of accurately identifying abnormal regions.

3. Method

3.1. Overview

Our GRCSF is a dual-feature compensation framework based on an encoder-decoder architecture. The training process involves first using a pre-trained MAE model to process input images and generate two sets of SSL residual maps with mask ratios of 50% and 75%. Subsequently, the input images and their corresponding SSL residual maps are simultaneously processed through a UNet++ backbone to produce the final segmentation results.

In the encoder, raw images are processed to extract hierarchical features. The GCU is introduced at each layer to recover pixel-wise information that is lost during downsampling. It does this by assigning higher weights to affected regions during feature concatenation between the encoder and the decoder, thereby enhancing the global feature representation. In the decoder, the RCU fuses multi-ratio residual maps (MRM) with upsampling features in the last three layers to highlight pixel-level discrepancies that likely correspond to lesions. The RCU processes these MRM using cross-attention and a patch-based mechanism that calculates importance scores, quantifying the likelihood that each patch contains lesions. By combining the complementary

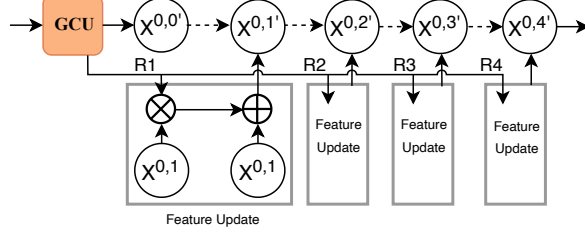


Figure 2: Details of skip pathway of UNet++. The skip connection features are updated using the GCU, where $X^{0,0'}$ represents the updated feature output from the GCU of the original skip feature $X^{0,0}$. Subsequently, $X^{0,1'}$, $X^{0,2'}$, $X^{0,3'}$, $X^{0,4'}$ are the updated features generated by incorporating the residuals from the GCU, followed by the operations illustrated in the figure. This process is applied to each skip concatenation layer in UNet++.

strengths of raw image features and MRM, GRCSF integrates global and regional information to improve segmentation accuracy, particularly for challenging lesions. The overall architecture is illustrated in Fig. 1.

3.2. Global Compensation Unit

The GCU addresses pixel-level information loss caused by downsampling in U-shaped CNN architectures by reintroducing lost details into the skip-concatenated features. During downsampling, the input feature map undergoes two convolutional operations, resulting in a downsampled feature map $S \in \mathbb{R}^{H \times W \times C}$. To mitigate information loss, S is re-upscaled to match the resolution of the skip feature map from the previous layer, $F \in \mathbb{R}^{H \times W \times C}$, producing $RU \in \mathbb{R}^{H \times W \times C}$. A comparison between RU and F identifies regions of information loss.

To refine RU , it is multiplied by the corresponding upsampled feature map $U \in \mathbb{R}^{H \times W \times C}$ in the decoder, which is enhanced by a Squeeze-and-Excitation (SE) mechanism [39]. The SE block, applied to both F and U , focuses on critical regions while suppressing irrelevant areas. This process yields two key outputs:

The skip-concatenation residual map is defined as:

$$R = \text{CS}(RU \otimes \text{SE}(U), \text{SE}(F)) \quad (1)$$

The updated skip-concatenation features are defined as:

$$C = \text{CS}(RU \otimes \text{SE}(U), \text{SE}(F)) \otimes F \oplus F \quad (2)$$

Here, $SE(U)$ and $SE(F)$ are attention maps generated by the SE block. \otimes and \oplus denote the element-wise product and addition, respectively. Each position can capture contextual information in the horizontal and vertical directions. The residual map R highlights areas of significant change and is particularly relevant for architectures such as UNet++, where each layer involves multiple skip concatenation features. For simpler architectures such as UNet, the residual map R is not required, as the updated skip feature C alone is sufficient to perform skip concatenation between the encoder and decoder.

By improving the information flow (Fig. 2) between the encoder and decoder, the GCU ensures better preservation of global and pixel-level details. It can be integrated into any U-shaped CNN, enhancing feature representations.

3.3. Regional Compensation Unit

The RCU is designed to generate a weighted feature map $M \in \mathbb{R}^{H \times W \times C}$ by utilizing the MRM, combined with the upsampled feature U . These MRM provide complementary information that enhances the ability of the segmentation network to focus on regions with a higher likelihood of containing lesions.

3.3.1. Residual Maps from Self-Supervised Learning

To compute the SSL residual maps of MRM, we adopt a SSL strategy with Mask Auto-encoder illustrated in Fig. 1. We trained the input images with two different mask ratios: 50% and 75%. The 75% mask ratio is used as the default, while the 50% ratio is empirically chosen to capture sufficient image context. For each input image $I \in \mathbb{R}^{H \times W \times 1}$, the MAE produces reconstructed images under both masking conditions. To reduce randomness caused by mask configurations that may fail to cover lesion areas, the MAE model is applied five times per mask ratio, generating five reconstructed images per input. The reconstructions, denoted as $R_1^{(i)}$ and $R_2^{(i)} \in \mathbb{R}^{H \times W \times 1}$ ($i = 1, \dots, 5$), are averaged to produce more stable representations as $R_1 = \frac{1}{5} \sum_{i=1}^5 R_1^{(i)}$ and $R_2 = \frac{1}{5} \sum_{i=1}^5 R_2^{(i)}$.

The SSL residual maps RM_1 and RM_2 are computed by calculating the cosine similarity pixel-wise between the input image I and the averaged reconstructions R_1 and R_2 , respectively, and subtracting the result from 1. The pixel-wise cosine similarity between two images is defined as CS:

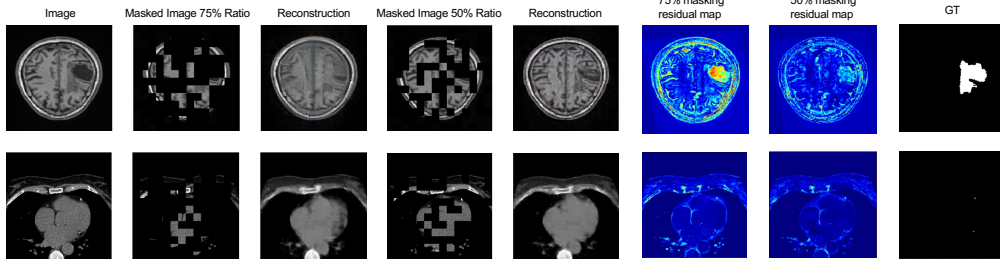


Figure 3: Example visualizations of MAE reconstruction results for mask ratios of 75% and 50%. The figure includes the masked input images, reconstructed images, derived MRM highlighting the differences between the original images and their reconstructions, and the corresponding ground truth for reference. Please zoom in for a clearer view.

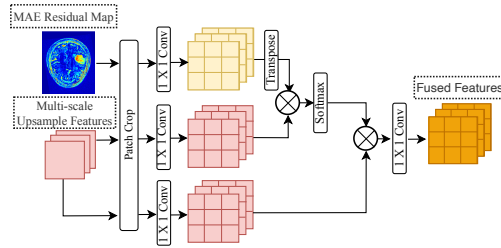


Figure 4: Patch-based cross-attention mechanism in the RCU module. This mechanism aligns upsampling features from the decoder layer with MRM at the same feature scales. The outputs are fused feature maps that combine information from both inputs.

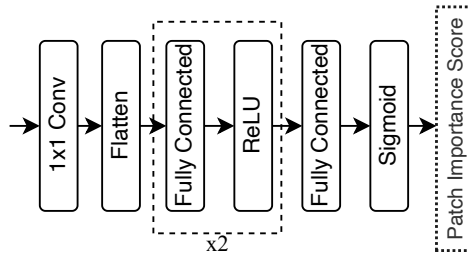


Figure 5: Regional importance scoring mechanism in the RCU module. This mechanism calculates the patch-based likelihood of lesion presence by processing decoder features generated by the backbone at each scale.

$$CS(I, R) = \frac{\sum_{x=1}^H \sum_{y=1}^W I(x, y)R(x, y)}{\sqrt{\sum_{x=1}^H \sum_{y=1}^W I(x, y)^2} \cdot \sqrt{\sum_{x=1}^H \sum_{y=1}^W R(x, y)^2}} \quad (3)$$

$$RM_1 = 1 - CS(I, R_1) \quad (4)$$

$$RM_2 = 1 - CS(I, R_2) \quad (5)$$

where (x, y) is pixel coordinates. This metric measures the cosine of the angle between the two vectors, quantifying their similarity on a scale from -1 to 1, where 1 indicates perfect alignment and -1 indicates complete opposition. These MRM highlight regions where the reconstructions differ from the original image, reflecting potential lesion areas (Fig. 3).

3.3.2. Regional Feature Fusion

To compute the weighted feature M , the RCU operates in a patch-based manner. The SSL residual maps RM_1 and RM_2 are divided into patches, resulting in patch-based representations $RM'_1 \in \mathbb{R}^{N \times P^2 \times C}$ and $RM'_2 \in \mathbb{R}^{N \times P^2 \times C}$, where $N = \frac{H}{P} \times \frac{W}{P}$ is the number of patches and $P \times P$ is the size of each patch. Similarly, the upsampled feature map U is reshaped into a patch-based representation $U' \in \mathbb{R}^{N \times P^2 \times C}$. Patch-based cross-attention is applied between RM'_1 , RM'_2 , and U' , respectively, enabling the MRM to highlight spatially relevant areas within U' . Cross-attention operations are represented as $(RM'_1 \otimes U')$ and $(RM'_2 \otimes U')$, where \otimes denotes the cross-attention mechanism described in [40] illustrated in Fig. 4.

Simultaneously, the patches in U' are processed through an importance score module shown in Fig. 5, which generates a score for each imaging feature patch as $\phi(U')$, where ϕ consists of a 1×1 convolution followed by two sets of fully connected layers with ReLU activations, an additional fully connected layer, and a sigmoid activation since multiple patches could contain lesions.

The cross-attention outputs are scaled by their corresponding importance scores and combined using learnable scalar weights W_1 and W_2 to produce the final feature map M . The computation is given by:

$$M = \varphi((RM'_1 \otimes U') \cdot \phi(U')) \cdot W_1 \oplus \varphi((RM'_2 \otimes U') \cdot \phi(U')) \cdot W_2 \oplus U \quad (6)$$

where φ is the operation to rearrange the feature map patches back to the original size in the backbone.

The weighted feature map M replaces U in the backbone segmentation network. Importance scores guide the network’s attention to patches that are more likely to contain lesions, while the patch-based cross-attention mechanism further refines these patches by emphasizing lesion-specific regional features.

3.4. Deployment and Objective Function

The GCU and RCU modules can be seamlessly integrated into any U-shaped CNN architecture that utilizes skip connections. Both modules offer flexibility and can be incorporated at various skip concatenation points or decoder layers, adapting to the specific needs of the backbone architecture and dataset characteristics. For the skip connections in the UNet++ backbone, the residuals from the first skip feature are added to subsequent skip connections, as illustrated in Fig. 2. The RCU generates a weighted feature map, which replaces the original upsampled feature map at the corresponding decoder layer.

The framework operates sequentially, with the MAE model first generating MRM from the input images. These MRMs are then used as additional information for the segmentation network, alongside the raw input images. The images are processed slice-wise, and the final output is a single-channel probability map of the same lateral resolution as the input images. A sigmoid activation function is applied to the output, producing per-pixel probabilities for the lesion and the background classification. The patch size of the MRM and the feature maps used in cross-attention are treated as tunable hyper-parameters, allowing optimization for different datasets. The MAE is trained using the Mean Squared Error (MSE) loss as default. For the segmentation network, a mixed loss function combining dice loss [41] and focal loss [42] is utilized for the ATLAS dataset, while focal loss is applied for the orCaScore dataset. This approach balances segmentation precision and recall, enhances sensitivity to challenging lesions, and addresses class imbalance. The mixed loss and focal loss are defined as follows:

$$\text{Loss}_{\text{ATLAS}}^{\text{mix}} = 1 - \frac{2|x \cap y|}{|x| + |y|} - \alpha(1 - p_t)^\gamma \log(p_t) \quad (7)$$

$$\text{Loss}_{\text{orCaScore}}^{\text{focal}} = -\alpha(1 - p_t)^\gamma \log(p_t) \quad (8)$$

where x and y are the target pixels in the predicted and ground truth (GT) images. α is a weighting factor, $p_t \in [0, 1]$ is the model’s estimated probability, γ is a focusing parameter, and we set $\alpha = 0.25$ and $\gamma = 2$ for both datasets.

This integration of the GCU and RCU into a U-shaped CNN backbone enhances the network’s ability to capture fine-grained details, improving sensitivity and segmentation performance for general segmentation tasks, especially for subtle and small lesions. The flexible design can easily be adaptable to other encoder-decoder backbone architectures, making the approach widely applicable.

4. Experiments

4.1. Datasets

We used two publicly available medical image segmentation datasets as examples to evaluate lesions with low-contrast and small-size characteristics: the Anatomical Tracings of Lesions After Stroke (ATLAS) v2.0 [43] dataset and the Coronary Artery Calcium Scoring (orCaScore) [44] dataset.

To evaluate segmentation performance on low-contrast lesions, we utilized the ATLAS 2.0 dataset, which comprises 955 samples of 655 public training cases and 300 hidden test cases with T1-weighted MRIs and manually segmented lesion masks, sourced from 33 research cohorts across 20 institutions worldwide. In our study, we used the 655 cases with publicly accessible MRIs and GT masks. The scans were acquired using 1.5-Tesla and 3-Tesla MR scanners, with most having high resolutions (1 mm³ or higher), except for four cohorts with at least one dimension between 1–2 mm³. The lesion annotation process employed ITK-SNAP for its semi-automated tool. Annotators were trained in neuroanatomy and standardized protocols, with quality control ensured through guidance from a neuroradiologist and extensive team feedback. Each lesion was traced twice to ensure consistency. The pre-processing involved intensity standardization and linear registration of T1-weighted images and lesion masks to the MNI-152 template using the MINC toolkit.

To evaluate segmentation performance on small lesions, we utilized the orCaScore dataset from the MICCAI 2014 Challenge on Automatic Coronary Calcium Scoring includes CT scans from 72 patients across four European academic hospitals, acquired using scanners from different vendors. Each patient has a non-contrast enhanced, ECG-triggered cardiac calcium scoring CT (CSCT) scan. Coronary artery calcifications (CAC) were manually annotated by an experienced radiologist and a physician. Annotations were provided for calcifications with in-plane resolutions of 0.4–0.5 mm and slice thicknesses/spacings of 2.5–3 mm. The dataset is divided

into 32 patients for training and 40 patients for testing (original set). However, GT masks are only available for the training set and not for the testing set. Therefore, we split the 32 patients in the training set into 26 for training, 5 for validation, and 1 for testing. In this study, after model building, the evaluation was performed using the original set of 40 patients for testing, by submitting segmentation results to the official dataset evaluation protocol [45].

4.2. Evaluation Setup

We used UNet++ as our segmentation model baseline due to its enhanced performance compared to U-Net in the two segmentation tasks evaluated in this study. To evaluate the performance of the GRCSF, we compared it against several state-of-the-art CNN and transformer-based methods commonly used in medical image segmentation: U-Net and UNet++, which utilize skip connection to enhance multi-scale features; Deeplabv3, which introduces various receptive fields to obtain better spatial information; TransUNet and SwinUNet, which take advantage of self-attention mechanism for better global context; and SPiN which is specifically developed for stroke lesion segmentation. All methods were trained and tested on the same datasets for a fair comparison. The comparison results for the ATLAS and orCaScore datasets are presented in Table 1.

To investigate the contributions of different components in GRCSF, we conducted ablation studies using the ATLAS dataset and UNet++ as the backbone architecture. These experiments aimed to assess the performance improvements introduced by the proposed modules of GCU, RCU and Importance Scoring mechanism. The GCU was applied at each skip connection layer in the backbone, although it can be adjusted depending on the task. Similarly, the RCU was applied to the last three upsampling layers in this study, but it can be selectively disconnected from specific layers as required. The results are summarized in Table 2.

For the ATLAS dataset, the four-subset design was implemented to evaluate the generalizability of the models across different medical centers and scanners while using relatively small amounts of training data compared to perform cross-validation on the entire dataset. The primary performance metric for the ATLAS dataset segmentation was the Dice Similarity Coefficient (DSC), which quantifies the similarity between the predicted and GT regions. Additionally, the Intersection over Union (IoU) was used to measure the overlap between the predicted and GT regions, while the F1 score highlighted the balance between precision and recall. Precision and

recall scores were also reported. All metrics were computed on a pixel-wise basis per patient to ensure precision in the evaluation.

The orCaScore evaluation framework is a publicly accessible, web-based protocol for algorithm evaluation, originally introduced at the MICCAI 2014 workshop in Boston, USA. This framework evaluates algorithms based on the number and volume of identified calcifications on a per-patient basis. For this study, the test results were post-processed according to specific guidelines: coronary calcifications were defined as connected voxel groups (using 3D 6-connectivity) with intensities exceeding 130 Hounsfield Units (HU) [46].

4.3. Implementation Details

For the ATLAS dataset, the 655 cases were divided into four subsets, which is similar to the data split in [47], with each subset containing patients from distinct cohorts. Within each subset, patients were further split into training and testing sets, with 80% allocated for training and 20% for testing. In particular, test patients were drawn from cohorts different from those in the training set. The pre-trained MAE model, enhanced with an additional GAN loss for more realistic generation (ViT-Large architecture, training mask ratios of 50% and 75%), was trained using all non-lesion training slices from all subsets. The training process was conducted over 500 epochs with a batch size of 64. The Adam optimizer [48] was utilized to minimize MSE loss, with an initial learning rate of 0.001. The learning rate decayed by a factor of 0.9 every 50 epochs to ensure stable convergence. The segmentation model was trained with an input size of 233x197 using the early stopping strategy, which stops training if the validation loss did not decrease for 15 consecutive epochs. A batch size of 21 was used, and the Adam optimizer was employed with an initial learning rate of 0.0001. Optimization incorporated a cosine warmup schedule [49] during the first 5 epochs, where the learning rate increased 10 times. The first and second moment estimates for the optimizer were set to 0.9 and 0.999, respectively. The weights of the convolutional filter were initialized using the He method [50], and the biases were initialized to zero. For the cross-attention operation in the RCU module, the feature patch sizes at the last three decoder layers were configured as 16x16, 16x16 and 32x32, respectively.

For the orCaScore dataset, following the data split described in the method section, the same pre-trained MAE models were trained using all non-lesion training slices over 200 epochs with a batch size of 8. The Adam optimizer was employed to minimize the MSE loss, starting with an initial learning rate of 0.001, which decayed by a factor of 0.9 every 50 epochs. The segmentation

network training followed the same configuration as for the ATLAS dataset, with the following adjustments: an input size of 512×512 , a smaller batch size of 2 due to computational resource constraints and a reduced initial learning rate of 0.0001. Additionally, the learning rate decayed by a factor of 0.5 if the validation loss did not decrease over 5 consecutive epochs. The RCU was presented in the last three decoder layers, the feature patch sizes were configured as 16×16 , 32×32 and 32×32 , respectively.

All experiments were conducted on a NVIDIA RTX A6000 Ada GPU and Pytorch version 2.0.0.

4.4. Results

4.4.1. State of the Art comparisons

For the ATLAS dataset, our GRCSF achieved a DSC of 0.422, outperforming the previous state-of-the-art method DeepLabv3, which ranked second, by 2.7% (Table 1). Additionally, our method demonstrated dominant performance across other metrics, achieving an IoU of 0.319 and an F1 Score of 0.473, representing improvements of 1.5% and 0.8% over the second-highest metrics achieved by TransUnet for IoU and DeepLabv3 for F1 Score, respectively.

Methods	ATLAS					orCaScore				
	Dice	IOU	F1	Precision	Recall	F1 volume	Sens vol	PPV vol	Sen lesion	PPV lesion
UNet	0.372	0.276	0.430	0.418	0.444	0.924	0.971	0.881	0.871	0.841
UNet++	0.381	0.286	0.440	0.409	0.476	<u>0.937</u>	0.954	0.920	0.801	0.880
DeepLabv3	<u>0.395</u>	0.295	<u>0.465</u>	0.413	0.531	0.936	0.929	0.944	0.516	0.925
SwinUnet	0.281	0.204	0.338	0.271	0.450	0.370	0.251	0.701	0.275	0.584
TransUnet	0.394	<u>0.304</u>	0.440	0.455	0.427	0.770	0.673	0.902	0.149	0.840
SPiN	0.376	0.288	0.427	0.404	0.453	0.913	0.896	<u>0.930</u>	0.253	0.892
GRCSF (Ours)	0.422	0.319	0.473	<u>0.451</u>	<u>0.497</u>	0.946	<u>0.962</u>	<u>0.930</u>	<u>0.827</u>	<u>0.899</u>

Table 1: Comparison of seven segmentation methods on the test sets of ATLAS and orCaScore datasets. The best results are highlighted in bold, and the second-best results are underlined. The metrics for ATLAS represent the average across four test subsets, while the metrics for orCaScore are derived from the online evaluation framework.

Selected example segmentation results from ATLAS and orCaScore images are shown in Fig. 6 and Fig. 7. The ATLAS results in Fig. 6 demonstrate the effectiveness of GCU and RCU, as

Methods	Dice	IOU	F1	Precision	Recall
UNet++	0.381	0.286	0.440	0.409	0.476
GRCSF w/o RCU	0.394	0.294	0.453	0.426	0.485
GRCSF w/o Importance Score in RCU	0.408	0.306	0.457	0.439	0.478
GRCSF	0.422	0.319	0.473	0.451	0.497

Table 2: Ablation study results on the 4 test sets of the ATLAS dataset. The best results are highlighted in bold. Metrics are obtained by averaging the results across the 4 test sets.

most methods tended to under-segment for challenging cases, whereas our method successfully captured the structures that other methods missed. The orCaScore results include both post-processed and non-post-processed visualizations of the same prediction, providing additional insights into model performance. In Fig. 7a, the post-processed results of all methods demonstrate accurate lesion boundaries in certain methods; however, this improvement is partly due to the removal of calcifications with image pixel values below 130HU during post-processing. This artificially improves the appearance of over-segmentation methods like U-Net and DeepLabv3, masking their inherent limitations. In contrast, the non-post-processed results in Fig. 7b reveal GRCSF’s true advantage of accurately segmenting small calcifications (as highlighted by the green arrows in Fig. 7) without significant over-segmentation. This highlights our model’s ability to capture challenging structures while maintaining recall without relying on post-processing.

The impact of integrating MRM on segmentation performance is illustrated in Fig. 8. The segmentation of the challenging lesion improved consistently when MRM was incorporated, particularly when using UNet++ as the backbone. This configuration showed the best performance across both datasets.

Segmentation outputs from UNet++ revealed common errors, such as completely missing small lesions and under-segmentation (false negatives) for lesions with subtle appearance. Low imaging contrast or insufficient global context often led to these inaccuracies. In contrast, the proposed method with MRM guidance avoided these problems and produced more accurate segmentations.

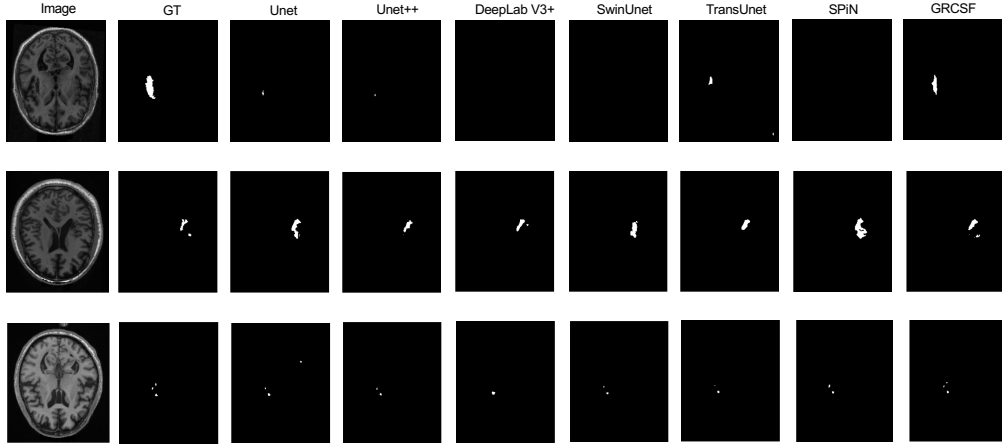


Figure 6: Visual comparison of our proposed method GRCSF against previous state-of-the-art at medical image segmentation using ATLAS dataset. Please zoom in for a clearer view.

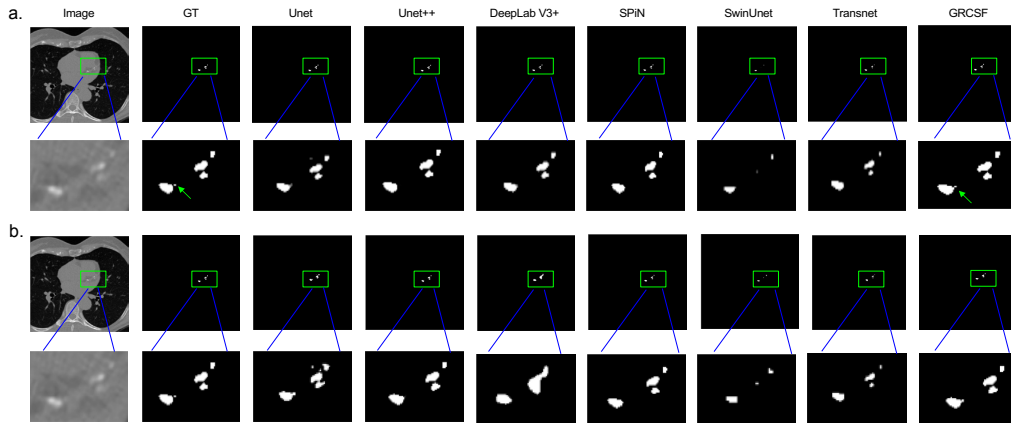


Figure 7: Visual comparison of our proposed method GRCSF, against previous state-of-the-art methods in medical image segmentation using the orCaScore dataset. (a) Visualization of predictions after post-processing, leveraging domain knowledge that calcifications are identified as regions where the predicted image pixel values exceed 130 HU. (b) Visualization of raw predictions without post-processing. Please zoom in for a clearer view.

4.4.2. Ablation Study

Adding the GCU to skip connections improved DSC and Precision by 1.3% and 1.7%, respectively from the UNet++ baseline (Table 2). The RCU introduced two key operations: (1) applying cross-attention between decoder feature maps and the MRM, and (2) generating patch-

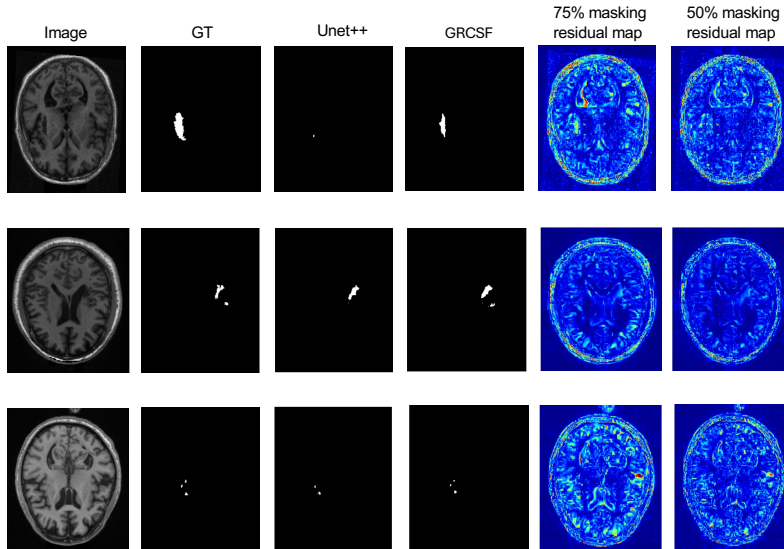


Figure 8: Example outputs from UNet++ and our proposed method GRCSF for the ATLAS dataset. The figure includes GT segmentations and the corresponding MRM of the input images for comparison. Please zoom in for a clearer view.

based importance scores. Building on the GCU results, adding cross-attention with MRM further improved DSC and Precision by another 1.5% and 1.3%. Incorporating patch-based importance scores provided an additional boost of 1.4% and 1.3%.

Overall, GRCSF improved DSC, IoU, F1, Precision, and Recall by 4.1%, 3.3%, 1.8%, 2.1%, and 4.2%, from the baseline, respectively. These results demonstrate that the integration of all proposed modules significantly enhances the framework’s segmentation performance, validating the design choices of GRCSF.

5. Discussion

Our results indicate that GRCSF consistently delivers superior segmentation performance across diverse datasets by leveraging a dual-feature compensation strategy. It integrates global feature recovery through the GCU to address downsampling losses and enhances regional features with the RCU using SSL residual maps and a patch-based cross-attention mechanism. This design enables GRCSF to effectively handle general lesion segmentation, including challenging tasks such as low-contrast and small lesion segmentation.

CNN-based models like U-Net and UNet++ rely on fixed skip connections that cannot adaptively refine feature maps, resulting in the loss of detailed features. Their fixed receptive fields further limit their ability to capture global contextual information required for segmenting lesions of varying scales and locations. Consequently, U-Net tends to over-segment lesions or miss small lesions altogether. While UNet++ mitigates over-segmentation compared to U-Net, it still struggles to detect challenging lesions with sufficient sensitivity. Similarly, SPiN improves resolution by upsampling input images but struggles with accurate segmentation due to its tendency to over-segment, leading to false positives. SPiN lacks mechanisms to dynamically focus on critical regions, which further limits its precision in complex cases. GRCSF effectively addresses the limitations of the above-mentioned methods in challenging lesion segmentation tasks. It significantly improves sensitivity to small and low-contrast lesions by feature compensation. GRCSF also resolves the blurred edges and ambiguous segmentation common in the output produced by other methods. Additionally, by dynamically focusing on lesion-specific regions, GRCSF minimizes false positives, enhancing the reliability of segmentation results in complex cases. Transformer-based models such as TransUNet and SwinUNet attempt to capture long-range dependencies and enhance global spatial information. However, their patch-based designs often struggle to capture detailed context around small lesions and fail to provide sufficient edge precision, resulting in high false-negative rates. Additionally, these models are prone to overfitting and suboptimal results on small datasets such as orCaScore, reducing their practicality and generalizability. In contrast, GRCSF integrates global and regional features effectively without requiring complex parameter tuning. It achieves higher precision in lesion segmentation while avoiding over-segmentation. The model's superior performance, even without post-processing of orCaScore results, further highlights its practicality for real-world applications where post-processing conditions are often limited.

In particular, the ATLAS dataset posed unique challenges due to significant image variability, including differences in imaging protocols, scanner types, and cohort demographics across medical centers. In our study, certain subsets involved training on a few cohorts while testing on entirely different cohorts, reflecting differences in cohort characteristics. Despite these challenges, GRCSF demonstrated exceptional robustness, consistently achieving higher segmentation performance across all four subsets, thereby validating its strong generalizability under diverse training and testing conditions.

The observed improvements in the ablation study highlight the complementary roles of global and regional compensation in GRCSF. The effective utilization of pixel-level feature similarity from different sources helps the model focus on regions that are often overlooked. The 50% and 75% mask ratios in MAE generate complementary MRM, which are adaptively integrated through learnable weights. This integration dynamically highlights informative regions while suppressing irrelevant ones, thereby mitigating false negatives and false positives caused by reconstruction errors. By leveraging these MRM through the RCU, GRCSF prioritizes regions with high lesion likelihood and compensates for missed feature representations, which is particularly effective for low-contrast and small lesions. This demonstrates the added value of MRM in comparison to baseline networks, which exhibited suboptimal performance in these challenging scenarios.

Unlike traditional SSL methods that use MAE for pre-training, our method directly utilizes the reconstructed images to generate SSL residual maps. While involving domain and high-level image features, preserving more low-level and pixel-level information. This method aligns with the learnable and consistent anatomical structures across patients. These benefits are not achievable through pre-trained encoders alone. Moreover, averaging five runs of MRM generation mitigates the variability introduced by random masking, ensuring reliable guidance for the backbone. This strategy significantly improves segmentation accuracy and robustness, offering a novel way to integrate SSL into medical image analysis.

6. Conclusion

In this work, we propose GRCSF, a dual-feature compensation framework that leverages a U-shaped backbone and SSL residual maps to improve lesion segmentation. We evaluate its effectiveness using two example datasets representing low-contrast and small lesion segmentation tasks. The GCU mitigates information loss caused by downsampling in the encoder, enhancing global feature representation to improve boundary delineation and small lesion detection. The RCU integrates complementary pixel-level features from MRM, employing a patch-based importance scoring mechanism to localize lesions more effectively while reducing false positives. Together, GRCSF provides a robust and efficient solution, demonstrating improvement in challenging medical imaging segmentation tasks.

Limitation: Our method relies on MAE-generated residual maps, which can be computationally demanding. In addition, though the method performs well on two datasets, variations in imaging protocols across medical centers still present challenges for broader application. Future efforts should focus on reducing model complexity and improving generalizability by introducing model compression and domain adaptation techniques.

References

- [1] M. Khalifa, and M. Albadawy, "AI in diagnostic imaging: Revolutionising accuracy and efficiency," *Computer Methods and Programs in Biomedicine.*, vol. 5, pp. 100146, Mar. 2024.
- [2] D. García-Lorenzo, S. Francis, S. Narayanan, D. L. Arnold and D. L. Collins, "Review of automatic segmentation methods of multiple sclerosis white matter lesions on conventional magnetic resonance imaging," *Medical image analysis.*, vol. 17, no. 1, pp. 1-18, Jan. 2013.
- [3] J.H. V. Waesberghe, M.A. V. Walderveen, J.A. Castelijns, P. Scheltens, G.L. à Nijeholt, C.H. Polman, and F. Barkhof, "Patterns of lesion development in multiple sclerosis: longitudinal observations with T1-weighted spin-echo and magnetization transfer MR," *American journal of neuroradiology.*, 19(4), pp.675-683, 1998.
- [4] D. Birenbaum, L. W. Bancroft, and G. J. Felsberg, "Imaging in acute stroke," *Western Journal of Emergency Medicine.*, vol. 12, no. 1, pp. 67-76, Feb. 2011.
- [5] M. P. Paing, S. Tungjikusolmun, T. H. Bui, S. Visitsattapongse and C. Pintavirooj, "Automated segmentation of infarct lesions in T1-weighted MRI scans using variational mode decomposition and deep learning," *Sensors.*, vol. 21, no. 6, pp. 1952, Feb. 2021.
- [6] C. Wang, T. Xia, J. YH. Yang and J. Kim, "A Three-Stage Self Supervised Deep Learning Network for Automatic Calcium Scoring of Cardiac Computed Tomography Images," *2022 International Conference on Digital Image Computing: Techniques and Applications (DICTA)*, IEEE, pp. 1-7, Feb. 2023.
- [7] A. Gupta, K. Bera, E. Kikano, J. D. Pierce, J. Gan, M. Rajdev *et al.*, "Coronary artery calcium scoring: current status and future directions," *Radiographics.*, vol. 42, no. 4, pp. 947-967, Jun. 2022.
- [8] C. E. Cardenas, J. Yang, B. M. Anderson, L. E. Court and K. B. Brock, "Advances in auto-segmentation," *Seminars in radiation oncology.*, vol. 29, no. 3, pp.185-197, Jul. 2019.
- [9] Z. Chen, S. Gu, G. Lu, D. Xu, "Exploiting intra-slice and inter-slice redundancy for learning-based lossless volumetric image compression," *IEEE Transactions on Image Processing*, vol. 31, pp. 1697-1707, 2022.
- [10] K. O'Shea, "An introduction to convolutional neural networks," *arXiv preprint arXiv:1511.08458.*, Dec. 2015.
- [11] V. Badrinarayanan, A. Kendall, and R. Cipolla, "Segnet: A deep convolutional encoder-decoder architecture for image segmentation," *IEEE transactions on pattern analysis and machine intelligence.*, vol. 39, no. 12, pp. 2481-2495, Dec. 2017.
- [12] O. Ronneberger, P. Fischer, and T. Brox, "U-net: Convolutional networks for biomedical image segmentation," *Medical image computing and computer-assisted intervention—MICCAI 2015: 18th international conference, Munich, Germany, October 5-9, 2015, proceedings, part III 18*, ., pp. 234-241, Nov. 2015.

- [13] Z. Zhou, M. M. R. Siddiquee, N. Tajbakhsh and J. Liang, "Unet++: A nested u-net architecture for medical image segmentation," Deep Learning in Medical Image Analysis and Multimodal Learning for Clinical Decision Support: 4th International Workshop, DLMIA 2018, and 8th International Workshop, ML-CDS 2018, Held in Conjunction with MICCAI 2018, Granada, Spain, September 20, 2018, Proceedings 4., pp. 3-11, Sep. 2018.
- [14] L.-C. Chen, G. Papandreou, F. Schroff, and H. Adam, "Rethinking Atrous Convolution for Semantic Image Segmentation," *arXiv:1706.05587*, 2017.
- [15] X. Lian, Y. Pang, J. Han and J. Pan, "Cascaded hierarchical atrous spatial pyramid pooling module for semantic segmentation," *Pattern Recognition.*, vol. 110, pp. 107622, Feb. 2021.
- [16] A. Vaswani, "Attention is all you need," *Advances in Neural Information Processing Systems.*, 2017.
- [17] J. Chen, J. Mei, X. Li, Y. Lu, Q. Yu, Q. Wei *et al.*, "Transunet: Transformers make strong encoders for medical image segmentation," *Medical Image Analysis.*, vol. 97, pp. 103280, Oct. 2024.
- [18] Z. Chen, L. Relic, R. Azevedo, Y. Zhang, M. Gross, D. Xu, L. Zhou, and C. Schroers, "Neural video compression with spatio-temporal cross-covariance transformers," *Proceedings of the 31st ACM International Conference on Multimedia*, pp. 8543-8551, 2023.
- [19] H. Cao, Y. Wang, J. Chen, D. Jiang, X. Zhang, Q. Tian and M. Wang, "Swin-unet: Unet-like pure transformer for medical image segmentation," *European conference on computer vision.*, pp. 205–218, Feb. 2023.
- [20] Z. Liu, Y. Lin, Y. Cao, H. Hu, Y. Wei, Z. Zhang, S. Lin and B. Guo, "Swin Transformer: Hierarchical Vision Transformer using Shifted Windows," *Proceedings of the IEEE/CVF International Conference on Computer Vision (ICCV)*, 2021
- [21] B. Chen, Y. Liu, Z. Zhang, G. Lu and A. W. K. Kong, "TransAttUnet: Multi-Level Attention-Guided U-Net With Transformer for Medical Image Segmentation," *IEEE Transactions on Emerging Topics in Computational Intelligence*, pp. 55-68, Feb. 2024
- [22] G. Xu, X. Zhang, X. He and X. Wu. "LeViT-UNet: Make Faster Encoders with Transformer for Medical Image Segmentation." *Pattern Recognition and Computer Vision. PRCV 2023.*
- [23] Y. Gao, M. Zhou and D.N. Metaxas. "UTNet: A Hybrid Transformer Architecture for Medical Image Segmentation." *Medical Image Computing and Computer Assisted Intervention – MICCAI 2021.*, pp 61–71, 2021.
- [24] A. Wong, A. Chen, Y. Wu, S. Cicek, A. Tiard, BW. Hong and S. Soatto, "Small lesion segmentation in brain MRIs with subpixel embedding," *International MICCAI Brainlesion Workshop.*, pp. 75–87, Jul. 2022.
- [25] R. Krishnan, P. Rajpurkar and E. J. Topol, "Self-supervised learning in medicine and healthcare," *Nature Biomedical Engineering.*, vol. 6, no. 12, pp. 1346-1352, Aug. 2022.
- [26] T. Chen, S. Kornblith, M. Norouzi, G. Hinton, "A simple framework for contrastive learning of visual representations," *International conference on machine learning.*, vol. 119, pp. 1597-1607, Jul. 2020.
- [27] K. He, H. Fan, Y. Wu, S. Xie and R. Girshick, "Momentum contrast for unsupervised visual representation learning," *Proceedings of the IEEE/CVF conference on computer vision and pattern recognition.*, pp. 9729-9738, Jun. 2020.
- [28] X. Chen and K. He, "Proceedings of the IEEE/CVF conference on computer vision and pattern recognition," *Nature Biomedical Engineering.*, pp. 15750-15758, Jun. 2021.
- [29] K. He, X. Chen, S. Xie, Y. Li, P. Dollár and R. Girshick, "Masked autoencoders are scalable vision learners," *Proceedings of the IEEE/CVF conference on computer vision and pattern recognition.*, pp. 16000-16009, Jun.

2022.

- [30] X.Wang, S. Takaki, J. Yamagishi, S. King, K. Tokuda, "A Vector Quantized Variational Autoencoder (VQ-VAE) Autoregressive Neural F_0 Model for Statistical Parametric Speech Synthesis," *IEEE/ACM Transactions on Audio, Speech, and Language Processing.*, vol. 28, pp. 157-170, Oct. 2020.
- [31] H. Bao, L. Dong, S. Piao and F. Wei, "Beit: Bert pre-training of image transformers," *arXiv preprint arXiv:2106.08254.*, Sep. 2022.
- [32] Z. Chen, G. Lu, Z. Hu, S. Liu, W. Jiang, and D. Xu, "LSVC: A learning-based stereo video compression framework," *Proceedings of the IEEE/CVF Conference on Computer Vision and Pattern Recognition (CVPR)*, pp. 6073-6082, June 2022.
- [33] Z. Chen, L. Zhou, Z. Hu, and D. Xu, "Group-aware parameter-efficient updating for content-adaptive neural video compression," *Proceedings of the 32nd ACM International Conference on Multimedia*, pp. 11022-11031, 2024.
- [34] Y. Zou, J. Jeong, L. Pemula, D. Zhang and O. Dabeer, "Spot-the-difference self-supervised pre-training for anomaly detection and segmentation," *European Conference on Computer Vision.*, pp. 392-408, Nov. 2022.
- [35] C. Ouyang, C. Biffi, C. Chen, T. Kart, H. Qiu and D. Rueckert, "Self-supervised learning for few-shot medical image segmentation," *IEEE Transactions on Medical Imaging.*, vol. 41, no. 7, pp. 1837-1848, July. 2022.
- [36] C. J. Reed, X. Yue, A. Nrusimha, S. Ebrahimi, V. Vijaykumar, R. Mao *et al.*, "Self-supervised pretraining improves self-supervised pretraining," *Proceedings of the IEEE/CVF Winter Conference on Applications of Computer Vision.*, pp. 2584-2594, 2022
- [37] L. Zhou, H. Liu, J. Bae, J. He, D. Samaras and P. Prasanna, "Self pre-training with masked autoencoders for medical image classification and segmentation," *2023 IEEE 20th International Symposium on Biomedical Imaging (ISBI).*, Apr. 2023.
- [38] J. Zhuang, L. Wu, Q. Wang, V. Vardhanabhuti, L. Luo and H. Chen, "MiM: Mask in Mask Self-Supervised Pre-Training for 3D Medical Image Analysis," *arXiv preprint arXiv:2404.15580.*, Apr. 2024.
- [39] J. Hu, L. Shen and G. Sun, "Squeeze-and-excitation networks," *In Proceedings of the IEEE conference on computer vision and pattern recognition*, pp. 7132-7141, 2018.
- [40] H. Zhang, I. Goodfellow, D. Metaxas and A. Odena, "Self-attention generative adversarial networks," *International conference on machine learning.*, pp. 7354-7363, 2019.
- [41] F. Milletari, N. Navab, and SA. Ahmadi, "V-net: Fully convolutional neural networks for volumetric medical image segmentation," *2016 fourth international conference on 3D vision (3DV).*, Dec. 2016.
- [42] TY. Lin, P. Goyal, R. Girshick, K. He and P. Dollar. "Focal Loss for Dense Object Detection," *IEEE Transactions on Pattern Analysis and Machine Intelligence.*, pp. 1-1, 2018.
- [43] SL. Liew, B.P. Lo, M.R. Donnelly, A. Zavaliangos-Petropulu, J.N. Jeong, G. Barisano, A. Hutton *et al.*, "A large, curated, open-source stroke neuroimaging dataset to improve lesion segmentation algorithms," *Scientific data.*, vol. 9, no. 1, pp. 320, Jun. 2022.
- [44] J. M. Wolterink, T. Leiner, B. D. de Vos, J.L. Coatrieux, B.M Kelm, S. Kondo *et al.*, "An evaluation of automatic coronary artery calcium scoring methods with cardiac CT using the orCaScore framework," *Medical physics.*, vol.43, no. 5, pp. 2361-2373, Apr. 2016.
- [45] [online] Available: <https://orcascor.score.grand-challenge.org/>

- [46] N. Gogin, M. Viti, L. Nicodème, M. Ohana, H. Talbot, U. Gencer *et al.*, “Automatic coronary artery calcium scoring from unenhanced-ECG-gated CT using deep learning,” *Diagnostic and Interventional Imaging.*, vol. 102, pp. 683-690, Nov. 2021.
- [47] C. Özgün, A. Abdulkadir, S. S. Lienkamp, “3D U-Net: learning dense volumetric segmentation from sparse annotation,” *Medical Image Computing and Computer-Assisted Intervention–MICCAI 2016: 19th International Conference, Athens, Greece, October 17-21, 2016, Proceedings, Part II 19.*, pp. 424–432, Oct. 2016.
- [48] P. K. Diederik, “Adam: A method for stochastic optimization,” *arXiv preprint arXiv:1412.6980.*, 2014.
- [49] N. Katsura and F. Baldassarre, “Cosine Annealing with Warmup for PyTorch,” *Version 2.0.*, <https://github.com/katsura-jp/pytorch-cosine-annealing-with-warmup>.
- [50] K. He, X. Zhang, S. Ren and J. Sun, “Delving deep into rectifiers: Surpassing human-level performance on imagenet classification,” *Proceedings of the IEEE international conference on computer vision.*, pp. 1026-1034, 2015.